catalysts

MDPI

Article

Synthesis of Rape Pollen-Fe_2O_3 Biohybrid Catalyst and Its Application on Photocatalytic Degradation and Antibacterial Properties

Jialin Gu †, Yanping Ma †, Xinshang Li, Shuwen Li, Siyi Chen, Yuxuan Cao, Yifan Lu, Rui Zhang, Wenquan Zhou, He Wang * and Jiangang Jiang *

College of Science, Northwest Agriculture and Forestry University, Xianyang 712100, China
* Correspondence: wanghenwafu@163.com (H.W.); jjg2100@163.com (J.J.)
† These authors contributed equally to this work.

Abstract: The efficient biohybrid photocatalysts were prepared with different weight ratios of Fe_2O_3 and treated rape pollen (TRP). The synthesized samples were characterized by different analytical techniques. The results showed that carbonized rape pollen had a three-dimensional skeleton and granular Fe_2O_3 uniformly covered the surface of TRP. The Fe_2O_3/TRP samples were used for degradation of Methylene Blue (MB) and Escherichia Coli (*E. coli*) disinfection in water under visible light. The degradation of MB and inactivation of *E. coli* was achieved to 93.7% in 300 min and 99.14% in 100 min, respectively. We also explored the mechanism during the reaction process, where reactive oxygen species (ROS) including hydroxyl radicals and superoxide radicals play a major role throughout the reaction process. This work provides new ideas for the preparation of high-performance photocatalysts by combining semiconductors with earth-abundant biomaterials.

Keywords: rape pollen; biohybrid materials; antibacterial; Fe_2O_3 nanoparticles; photocatalysts

check for updates

Citation: Gu, J.; Ma, Y.; Li, X.; Li, S.; Chen, S.; Cao, Y.; Lu, Y.; Zhang, R.; Zhou, W.; Wang, H.; et al. Synthesis of Rape Pollen-Fe_2O_3 Biohybrid Catalyst and Its Application on Photocatalytic Degradation and Antibacterial Properties. *Catalysts* **2023**, *13*, 358. https://doi.org/10.3390/catal13020358

Academic Editors: Xiangjiu Guan and Shichao Zong

Received: 25 December 2022
Revised: 26 January 2023
Accepted: 30 January 2023
Published: 6 February 2023

Copyright: © 2023 by the authors. Licensee MDPI, Basel, Switzerland. This article is an open access article distributed under the terms and conditions of the Creative Commons Attribution (CC BY) license (https://creativecommons.org/licenses/by/4.0/).

1. Introduction

In today's society, environmental problems are becoming more and more serious. The management of water pollution is inevitable, which includes organic dyes [1], heavy metals [2], antibiotics [3], and bacterial contamination [4]. This has become a major global governance problem that restricts the development of human society and endangers the ecological balance [5]. Among the traditional wastewater treatment processes are ozone nitration [6], chlorination [7], and ultraviolet irradiation [8], which inevitably have the disadvantages of secondary pollution, complicated operation, and high energy consumption. Photocatalytic technology stands out as a technology that has a high potential for development and uses as an application of solar energy as an energy source. Photocatalysis is one of the most promising technologies for solving ecological and energy problems due to its green, easy-to-operate, non-toxic, and harmless characteristics, and mild reaction conditions [9–11].

It has been found that semiconductor materials can effectively promote the photocatalytic decomposition of organic compounds, especially semiconductors with narrow band gaps (Fe_2O_3 [12], Bi_2O_3 [13], CdS [14]) that can absorb visible light [15]. Semiconductor materials can also kill bacteria such as *E. coli* and Staphylococcus aureus through the photocatalytic pathway [16,17]. Fe_2O_3, as an environmentally friendly n-type semiconductor with many advantages such as low cost, high visible light utilization, abundant storage content, and high stability, has been used in a large number of applications [18,19]. Although there are many advantages of Fe_2O_3 nanomaterials in the field of photocatalysis, the low electron mobility and short carrier diffusion lengths limit its industrial application mboxciteB20-catalysts-2151803,B21-catalysts-2151803,B22-catalysts-2151803. To solve these problems, many efforts, such as element doping [23], heterojunction construction [24],

morphology control [25], and co-catalyst modification [26], have been adopted. Among all of the strategies, heterojunction construction is an effective way that can take advantage of multiple materials at the same time to improve the performance of a photocatalyst [27–30]. Therefore, many researchers have focused on the combination of Fe_2O_3 and other semiconductors to form heterojunction, with promising results [31].

In recent years, carbon-based materials, such as carbon quantum dots [32,33], amorphous carbon [34], carbon nanotubes [35], and graphene [36], have widely developed owing to their high stability, good conductivity, and nontoxicity. In nature, there is a large amount of carbon materials with a three-dimensional structure that donate the photocatalyst with high surface-exposed active sites, resulting in higher photocatalytic efficiency in theory [37–39]. As a typical plant-based material, the unique structure of rape pollen not only provides sufficient active sites for the reaction, but also promotes the separation of photogenerated holes and electrons by reducing its diffusion length [40]. It is also characterized by low cost, a non-toxic nature, a simple synthesis process, and adjustable surface properties. It overcomes the disadvantages of conventional carbon-based photocatalysts prepared through complicated procedures and expensive chemical precursors. Therefore, multifunctional material substrates with high adsorption capacity and high photocatalytic degradation activity can be prepared from treated rape pollen.

In this work, a granular Fe_2O_3/C composite-based rape pollen was successfully synthesized by a simple hydrothermal method. This composite was assembled by attaching the granular Fe_2O_3 to the porous structure of carbonized rape pollen. By comparing with pure Fe_2O_3 samples, we demonstrated that the porous structure of carbonized pollen could effectively improve the contact area of Fe_2O_3 with methylene blue (MB) molecules and enhance the photocatalytic performance of MB degradation under visible light. Meanwhile, the sample was applied in *E. coli* inactivation in water, and the results showed that granular Fe_2O_3/C showed significant inhibition activity of *E. coli*. In addition, we also explored the generation of reactive oxygen species ROS during the degradation and *E. coli* inactivation process. Based on these results, the photocatalytic mechanism in the degradation of granular Fe_2O_3/C was finally proposed in this paper.

2. Results

2.1. Characterization of the Fe_2O_3/C Heterojunction

Figure 1 shows the SEM images and XRD patterns of all prepared samples. As Figure 1a shown, the TRP is generally oval with a homogeneous carbon skeleton and a unique three-dimensional hierarchical network structure. The size of TRP is about 28 μm in length and 15 μm in width. Moreover, TRP has plenty of pores with size ranges from 500 nm to 1 μm, which provides large contact area between photocatalyst and reactant. The intact morphology of the pollen within the pores indicates that the structure and integrity of the pollen is preserved throughout the carbonization process. After a subsequent hydrothermal process, there are tiny particles deposited on the TRP surface, which should be Fe_2O_3. However, the number of Fe_2O_3 particles is so small that most of the TRP surface is not covered (seen Figure 2b). When the ratio of Fe_2O_3 increases to 50% in precursor solution, it is clearly seen that almost every surface—even inside the pore—of TRP is covered uniformly by Fe_2O_3 particles, as seen in Figure 1c. The size of the synthesized granular Fe_2O_3 is uniform and around 50 nm, while the pore size structure of the carbonized rape pollen is still preserved, which is essential for absorption reactant in the follow-up photocatalytic reaction. When further increasing the ratio of Fe_2O_3 to 80% in precursor solution, only Fe_2O_3 particles without TRP can be seen in Figure 1d, implying all the pores of TRP have been occupied by Fe_2O_3 particles, which will reduce the area between catalyst and reactant. Finally, pure Fe_2O_3 particles are prepared as comparison, as seen in Figure 1e. Subsequently, the XRD data are conducted to further determine structure of samples. As Figure 1f shown, TRP just has a wide diffraction peak at 22°, indicating the formation of an amorphous structure, which is consistent with other reports [41]. After Fe_2O_3 is deposited on the TRP surface, many new peaks are displayed in the XRD pattern. The new peaks at 24.16°, 33.28°,

35.74°, 40.99°, 49.50°, 54.23°, 62.26°, and 64.18° correspond to the (012), (104), (110), (113), (024), (116), (214), and (300) crystallographic plane for Fe_2O_3, respectively (JCPDS Card No. 00-001-1053), which proves Fe_2O_3 has been deposited on the TRP surface successfully. No other impurities are found in the XRD pattern. Thus, we can conclude that pure samples are fabricated via the simple hydrothermal method.

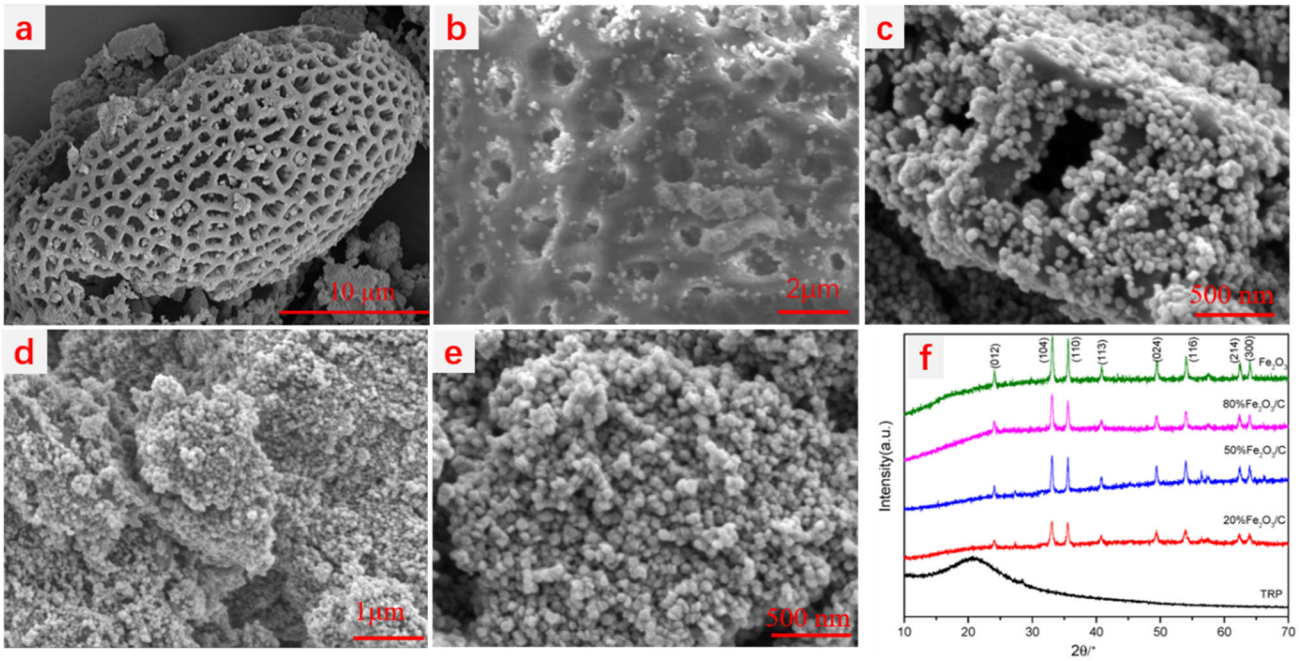

Figure 1. SEM images of (**a**) treated rape pollen, (**b**) 20% Fe_2O_3/C, (**c**) 50% Fe_2O_3/C, (**d**) 80% Fe_2O_3/C, (**e**) Fe_2O_3, and (**f**) XRD patterns of all samples.

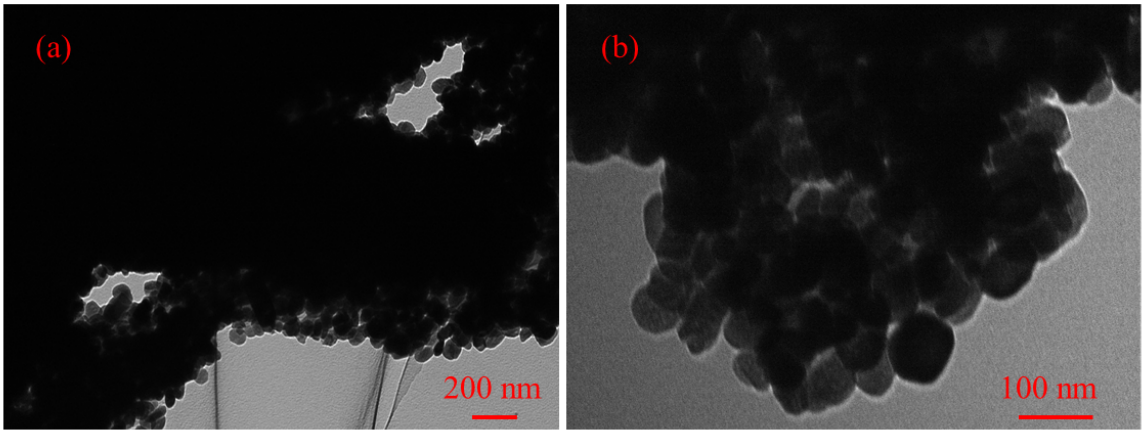

Figure 2. (**a**) TEM and (**b**) HRTEM image of 50% Fe_2O_3/C.

The structure of the 50% Fe_2O_3/C is further demonstrated by its TEM image in Figure 2. It is clear seen that the granular Fe_2O_3 is well loaded on the surface and inside the hole of carbonized rape pollen. The size of the granular Fe_2O_3 is evaluated to be ~50 nm. Meanwhile, the pore structure of the carbonized rape pollen can be clearly observed in Figure 2a, which is consistent with the SEM results.

In order to obtain the specific surface area and pore size of the samples, N_2 adsorption–desorption analysis is performed. As shown in Figure 3a, the specific surface area of 50% Fe_2O_3/C is the largest in three composites, indicating that the increase in the moderate amount of Fe_2O_3 particles is beneficial to increase the specific surface area, while too much Fe_2O_3 leads to the complete coverage of the carbonized pollen and the decrease in specific

surface area. From Figure 3b, it can be seen that the pore size of this composite catalyst is mainly mesoporous with a pore diameter of about 25 nm, and also contains a small amount of macropores, which is consistent with the SEM and TEM results. At the same pore size, the pore area of 50% Fe_2O_3/C is much larger than the other two.

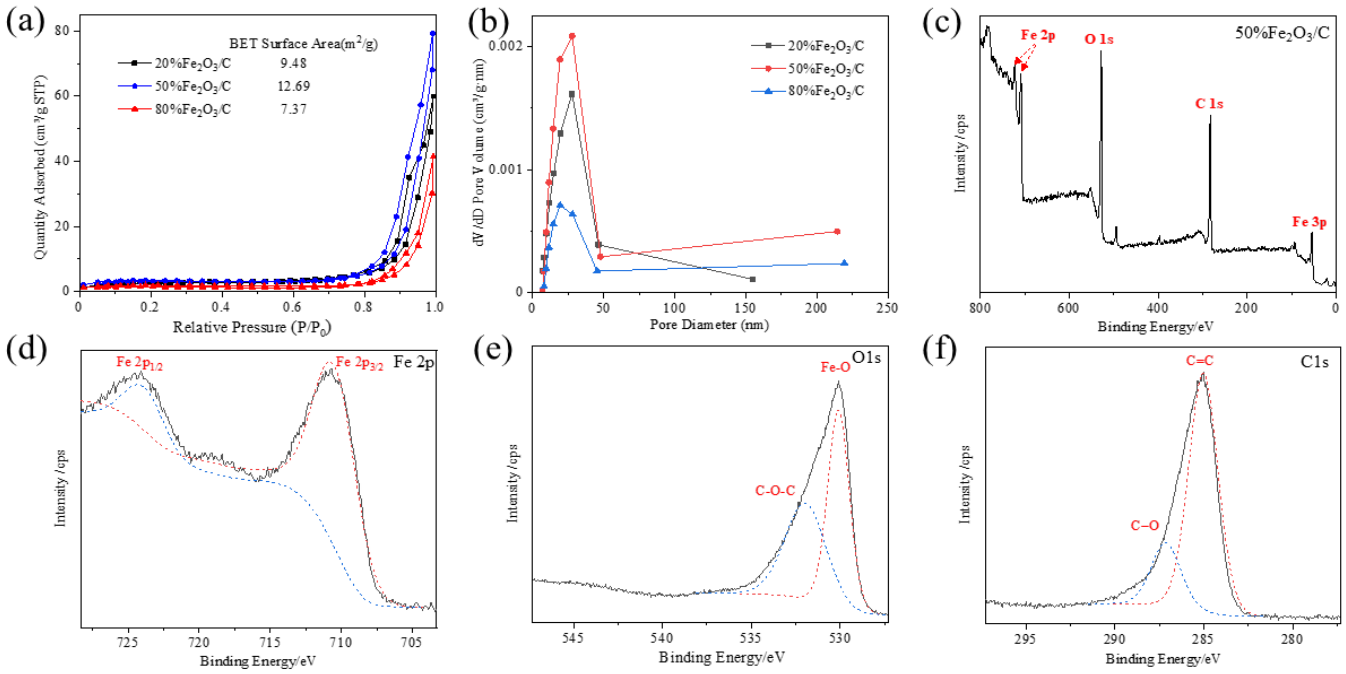

Figure 3. (**a**) N_2 adsorption isotherms, (**b**) pore size distribution curves of different ratios of Fe_2O_3/C samples, (**c**) full XPS spectra of 50% Fe_2O_3/C, high-resolution XPS spectra of (**d**) Fe 2p, (**e**) O 1s, and (**f**) C 1s.

The chemical state of 50% Fe_2O_3/C is analyzed by XPS. Figure 3c shows that the catalyst consists of three elements, Fe, O, and C. The binding energy of each element also corresponds to the results of previous studies [42]. Among them, the chemical states of each element are described as follows: Fe has mainly spin-orbit peaks of $Fe2p_{1/2}$ and $Fe2p_{3/2}$ with binding energies of 724.2 eV and 710.7 eV [43], respectively (see Figure 3d). O1s binding energy at 529.5 eV is attributed to Fe_2O_3 with Fe-O bonding [44], and the binding energy at 531.8 Ev corresponds to the surface chemisorbed oxygen functional group (C-O-C) (see Figure 3e). The two binding energies of 284.6 eV and 287.2 eV for C1s demonstrate the presence of C=C and C-O in this composite [45].

2.2. Optical Property of Samples

The optical properties of Fe_2O_3, TRP, 20% Fe_2O_3/C, 50% Fe_2O_3/C, and 80% Fe_2O_3/C are recorded over a wavelength range from 300 to 800 nm. As Figure 4 shown, the absorption edge of pure Fe_2O_3 is about 590 nm, corresponding to a band gap energy of 2.1 eV, which is calculated by the Kubelka-Munk method [46]. When Fe_2O_3 is deposited on the TRP, an obvious red shift of the absorption edge is observed in Figure 4. Meanwhile, the absorption intensity in the infrared region (IR) gradually increases with TRP weight ratio increases in the composite. Other researchers have also reported these phenomenon-based carbon materials [47]. They proposed that the red shift of absorption suggested the interfacial interactions between the carbon and other materials, and the IR absorption was mainly caused due to the light absorption of carbon materials. Based on the above results, it is demonstrated that Fe_2O_3 and TRP have tightly integrated and greatly extend the light absorption range of Fe_2O_3 due to the introduction of TRP. It is worth mentioning that the light energy in the infrared region may not drive the reaction of MB degradation and *E. coli* inactivation via photo dynamic effect, but it may favor the reaction of MB degradation and

E. coli inactivation via photo thermal effect. We will test the hypothesis in the antibacterial activity section.

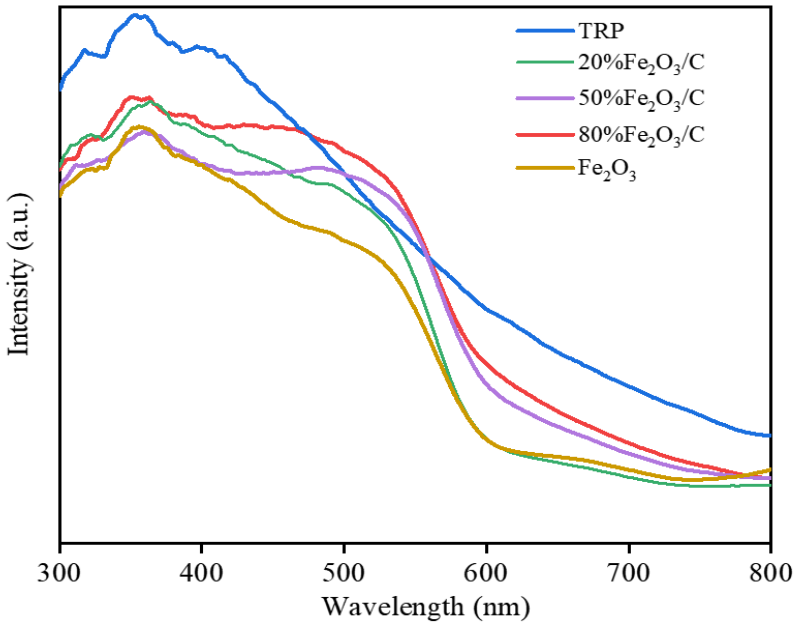

Figure 4. UV–vis diffuse reflection spectra of Pure Fe_2O_3, TRP and 20%, 50%, 80% Fe_2O_3/C samples.

2.3. Photocatalytic Activity of Degrade Methylene Blue

In a previous article reported on rape pollen, sulfuric acid-treated rape pollen samples showed a rather high adsorption of MB. To avoid the influence of adsorption on the experimental results, the suspension of samples and MB solution was formulated, and then stirred in the dark for 1 h to reach adsorption equilibrium. The photocatalytic activity of the xFe_2O_3/C samples was evaluated by degradation the MB as shown in Figure 5a. The photocatalytic activity of xFe_2O_3/C samples increases and then decreases with the Fe_2O_3 content increased. The 50% Fe_2O_3/C sample shows the highest photocatalytic activity for MB degradation. In the present experiment, we compare the degradation activity of 50% Fe_2O_3/C at a controlled and uncontrolled temperature, denoted as 50% Fe_2O_3/C (PC) and 50% Fe_2O_3/C (PC/PT) in Figure 5a, respectively. It can be found that 50% Fe_2O_3/C (PC/PT) shows higher degradation activity than 50% Fe_2O_3/C (PC). The possible reason for this is that TRP can absorb IR light irradiation and gives off heat, resulting in the temperature of the reaction system rising, and promoting the reaction process. In fact, we observed that the temperature of reaction system rose from 59.8 °C to 63.2 °C without and with 50% Fe_2O_3/C in solution, which proved the photothermal effect of TRP. Meanwhile, the primary kinetic curve of photocatalytic degradation of MB is calculated by the following equation [48]:

$$ln(C_0/C_t) = kt \quad (1)$$

where, C_0 is the initial concentration of MB, C_t is the concentration of MB dyes at varied time, t and k referred irradiation time and rate constant, which derives from MB (absorption maxima at 664 nm) with respect to time. The primary kinetic curve is shown in Figure 5b. The reaction rate constants (k) for all photocatalysts is determined from the slope of fitted curves. All the plots show a linear relationship with good correlation coefficients (R^2 = 0.99), and the highest removal rate (k = 0.0949 min^{-1}) is obtained by 50% Fe_2O_3/C. The reason that 50% Fe_2O_3/C gives the highest activity may derive from its unique structure. Based on the SEM, TEM, and BET results, 50% Fe_2O_3/C has a hierarchical structure with abundance pores and Fe_2O_3 particles, which provide a large surface to absorb organic molecules and then accelerate the degradation rate of MB. Further, the ratio of Fe_2O_3 exceeds 50% in composite, so part of or all the pores will be occupied by Fe_2O_3 particles, which reduces

the contact area between catalyst and reactant. Thus, 80% Fe_2O_3/C and pure Fe_2O_3 show lower activity than that of 50% Fe_2O_3/C. On the other hand, 20% Fe_2O_3/C and pure TRP display insufficient use of photogenerated charges, leading to lower performance.

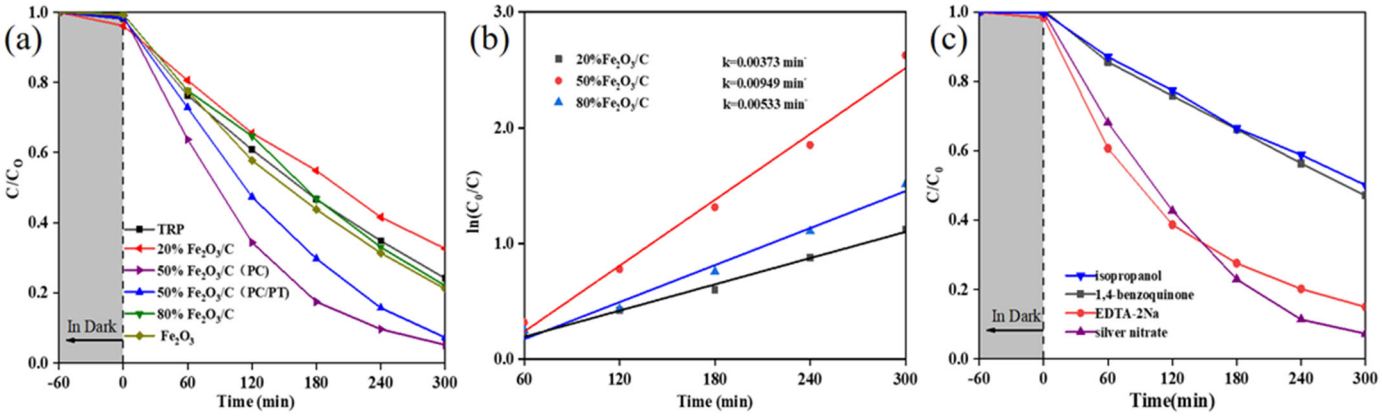

Figure 5. (**a**) Photocatalytic degradation of MB over TRP, 20%, 50%, 80% Fe_2O_3/C and Fe_2O_3 composites under visible and infrared light irradiation. (**b**) Corresponding pseudo first-order plots and (**c**) photo degradation of MB over as−synthesized 50% Fe_2O_3/C composite in the presence of different scavengers.

Figure 5c shows the effect of different scavengers on the photocatalytic activity of the 50% Fe_2O_3/C sample on the degradation of MB. For the 50% Fe_2O_3/C photocatalytic system without a scavenger, the degradation rate of MB (20 mg/L) is 92.8% within 300 min under visible and infrared light irradiation. When silver nitrate and EDTA-2Na are added into the reaction system as the electron and hole scavenger, the degradation rate is almost unchanged, indicating that the electron and hole are not major reactive oxygen species in the degradation process, while $\cdot O_2^-$ and ·OH are strongly involved in the degradation process of MB. When 1,4-benzoquinone and isopropyl are added into the reaction system as $\cdot O_2^-$ and ·OH scavenger, the degradation activity of the sample decreases dramatically. This reveals that $\cdot O_2^-$ and ·OH play an important role in the degradation of MB.

2.4. Antibacterial Activity of Samples

E. coli is selected to investigate the photocatalytic antibacterial efficiency of 50% Fe_2O_3/C, because 50% Fe_2O_3/C gives the highest activity in the photocatalytic degradation of MB. We compared photocatalytic antibacterial activity of 50% Fe_2O_3/C with just the photocatalytic effect and with the photocatalytic–photothermal effect, denoted as 50% Fe_2O_3/C (PC) and 50% Fe_2O_3/C (PC/PT), mentioned in the photocatalytic activity of MB degradation. The antibacterial efficiency of 50% Fe_2O_3/C in dark, pure TRP and Fe_2O_3 in light irradiation is also record as the control group. Figure 6a shows the death rate of *E. coli* in different reaction conditions versus time. The trend shows that there is a time dependence of the death of *E. coli*. However, the death rate of *E. coli* decreases after more than 80 min, probably because the activity of the photocatalytic material decreases as the reaction proceeds, resulting from the nanoparticles undergoing electrostatic adsorption, agglomeration, and precipitation. The best photocatalytic antibacterial efficiency is achieved by 50% Fe_2O_3/C under photocatalytic–photothermal synergy (PC/PT), and the mortality rate of *E. coli* reaches 99.14%. While the mortality rate of *E. coli* is 52.54% for 50% Fe_2O_3/C under only photocatalytic conditions (PC). In comparison, the mortality rate of *E. coli* is only 17%~23% for 50% Fe_2O_3/C in dark, pure TRP and Fe_2O_3 under only photocatalytic conditions. Figure 6b,c show the plate colony plots of *E. coli* at different time points under PC and PC/PT conditions for 50% Fe_2O_3/C, respectively. From the graphs, it can be seen that the *E. coli* colonies in the plates are round, neatly edged, smooth, translucent, and evenly distributed. The graphs prove again that the total number of colonies decreases with

the reaction time prolongation, and 50% Fe_2O_3/C gives the best photocatalytic antibacterial efficiency under photocatalytic–photothermal synergy (PC/PT).

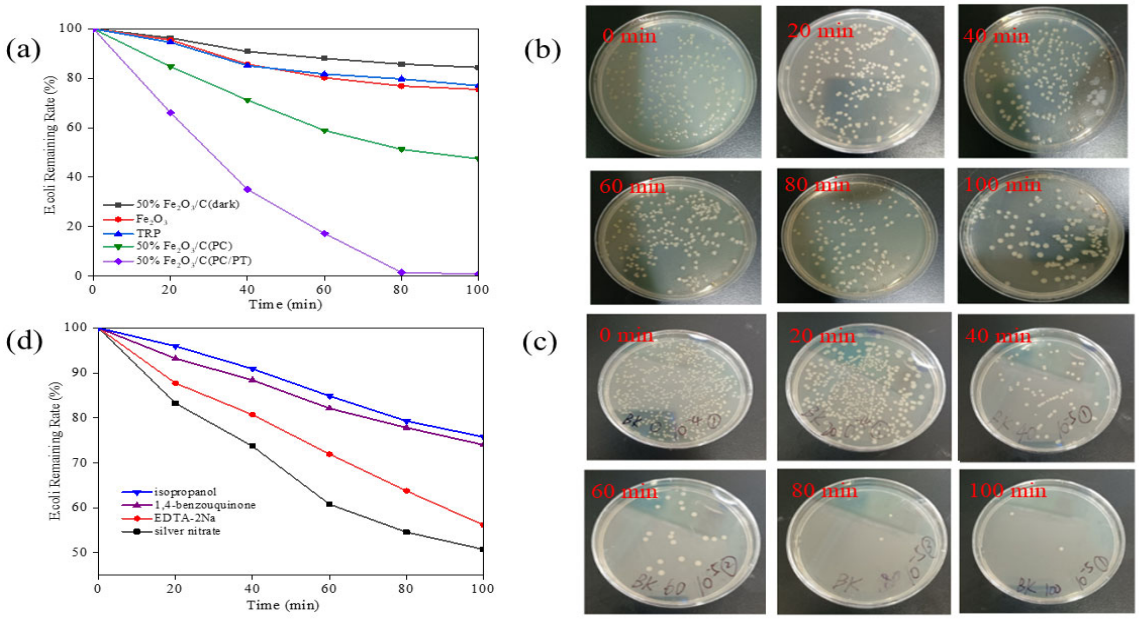

Figure 6. (**a**) Survival rate of *E. coli* in different reaction conditions versus reaction time. (**b**) Plates of colonies of *E. coli* at different time points for 50% Fe_2O_3/C under PC condition. (**c**) Plates of colonies of E. coli at different time points for 50% Fe_2O_3/C under PC/PT condition. (**d**) Photocatalytic inactivation of *E. coli* by 50% Fe_2O_3/C under free radical capture assay.

There is a significant difference of temperature in the sterilization rate under PC and PC/PT conditions. The temperature of the reaction system is maintained at 25 °C by applying a condensation system for the PC condition, while the temperature will increase to 68 °C at 100 min under PC/PT synergistic conditions. Other researchers have reported that the photothermal effect of material can accelerate charge transfer and enhanced photocatalytic activity [49,50]. In our study, TRP of composite can absorb IR light irradiation and produce heat, leading to a local temperature rise and then driving charge transfer to the surface of the catalyst. In this condition, more free radicals would be generated in the solution to kill the bacteria. Further, the high temperature itself will produce some damage to the bacteria [51]. Thus, the 50% Fe_2O_3/C gives the highest antibacterial efficiency under the combined photocatalytic and photothermal effect.

The results of the free radical capture test are shown in Figure 6d. It is known that the mortality rate of *E. coli* is 52.54% in 100 min in the absence of free radical capture, and the value decreases to 49.28% and 43.85% for the presence of electron and hole trapping agent, respectively. In addition, the mortality rate of *E. coli* decreases to 26% and 24.24% for presence of $\cdot O_2^-$ and ·OH trapping agent, respectively. This indicates that $\cdot O_2^-$ and ·OH play a key role in this photocatalytic reaction, which is consistent with the results of MB degradation in Figure 5c.

To further understand the antibacterial process, the morphology of *E. coli* in the photocatalytic procedure is recorded by SEM at different time points. As shown in Figure 7, when the photocatalytic reaction is not yet started, the *E. coli* is an intact rod-like structure, full of morphology and vigor. When the reaction time proceeds to 90 min, under the attack of free radicals, the polyunsaturated phospholipids of the cell membrane are oxidized, the cell activity decreases and begins to wilt, crumple, and partially rupture, and in some sites with more free radicals, the cells even have died partly. When the reaction time proceeds to 180 min, more free radicals generate, which will easily penetrate the cell membrane and enter the cell interior in the damaged state, and the redox reaction will occur with the proteins and polysaccharides in the cell, decomposing them into water, carbon dioxide,

and other small molecules. At that time, the cell membrane is completely ruptured, the lysate flows out of the cell, and the material is completely mixed together. The intact cell disappears in the SEM picture, and the cell is completely dead.

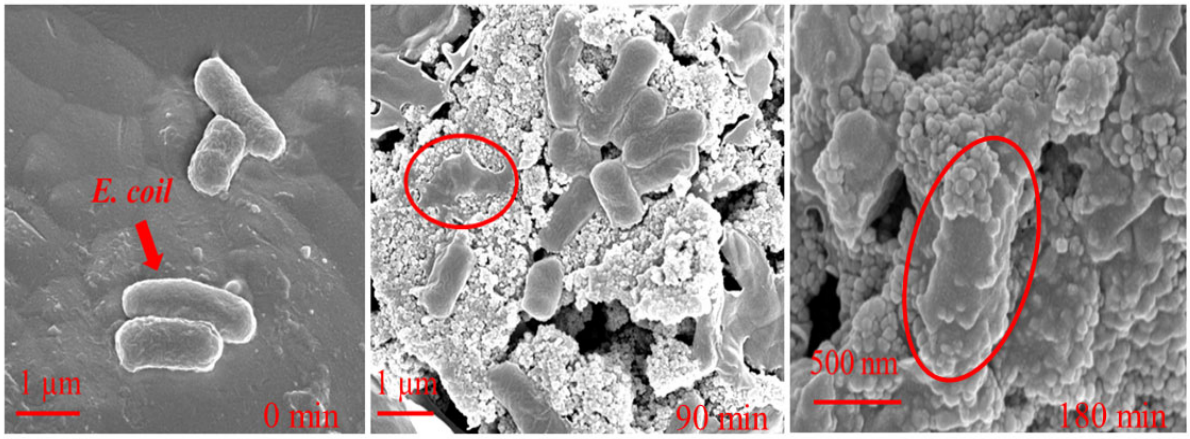

Figure 7. SEM images of *E. coli* at different time points for 50% Fe_2O_3/C under photocatalytic condition.

2.5. Mechanism

Based on the above results, we propose a possible mechanism of degradation of MB and antibacterial of samples, which is schematically proposed in Scheme 1. Fe_2O_3 has an energy band gap of 2.1 eV according to the above UV-vis result, while the band gap of TRP is 1.84 eV [52]. In the present experiment, Fe_2O_3 particles are deposited on the TRP to form a Fe_2O_3/C heterojunction, facilitating the separation and transport of photogenerated charges. Under light irradiation, Fe_2O_3/C will absorb photons with comparable or higher energy than its energy band gap and generate electrons and holes. Then, the photogenerated electrons in conduction band of Fe_2O_3 will rapidly transfer to the valance band of TPR driven by the internal electric field, which prevents the combination of electron–hole in Fe_2O_3/C bulk. Subsequently, the photogenerated charges on the surface of Fe_2O_3 and TRP will react with other substances in the system and induce ROS as follows.

$$h^+ + H_2O \rightarrow OH \quad (2)$$

$$h^+ + OH^- \rightarrow OH \quad (3)$$

$$e^- + O_2 \rightarrow O_2^- \quad (4)$$

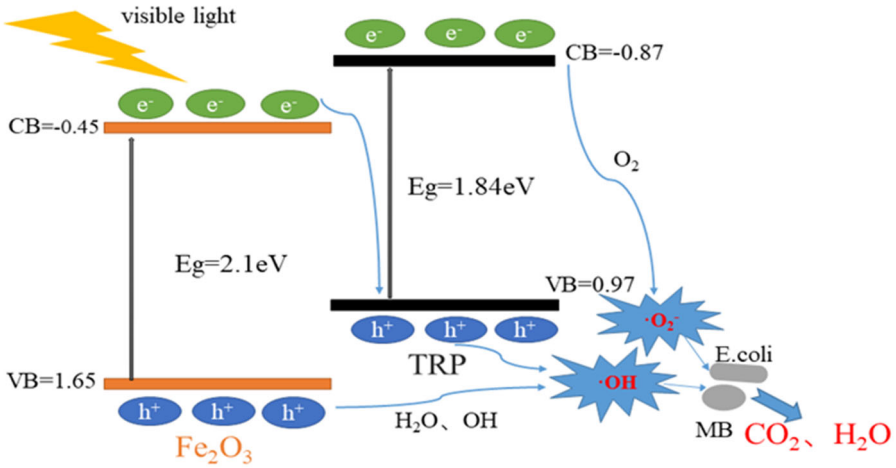

Scheme 1. Photocatalytic mechanism of Fe_2O_3/C catalysts under visible light irradiation.

According to the descriptions in Figures 5c and 6d, the ROS that play a major role in the photocatalytic degradation process are ·OH and $\cdot O_2^-$, which have a strong oxidizing capacity and will oxidize MB to small molecules or CO_2 and H_2O. For sterilization process, the free radicals will attack the outer cell membrane, leading to the oxidation of polyunsaturated phospholipids. Under continuous attack, the cell membrane structure and function are damaged. The destruction of the membrane allows for the oxidation and leakage of the cytoplasmic substances, ultimately resulting in the cell death.

It is worth mentioning that the efficiency of degradation MB and antibacterial *E. coli* under visible light is low compared to others' reports [53,54]. However, we demonstrate a simple method that Fe_2O_3 particles were deposited on the TRP with unique three-dimensional structure, which expands the range of applications for biomaterials. Furthermore, we find that the TRP of composite can absorb IR light irradiation and produce heat, leading to a local temperature rise and driving charge transfer to the surface of the catalyst. In this condition, more free radicals would be generated to kill the bacteria, which improves the efficiency of antibacterial *E. coli*, differing from previous work [55].

3. Materials and Methods

3.1. Preparation of Carbonized Rape Pollen Loaded with Granular Fe_2O_3

All chemical reagents were analytical grade and purchased from Sinopharm Chemical Reagent Co., Ltd. (Shanghai, China) without further treatment. First, the carbonized rape pollen was prepared as ref [56]. In a typical procedure, the nature rape pollen was immersed in absolute ethanol with ratio of 1:10 (w:v) under sonication to remove the cores and impurities. Then, rape pollen was poured into a 100 mL mixture of anhydrous ethanol and formalin with a volume ratio of 1:1 (pH = 7) overnight after washing with deionized (DI) water several times. After filtration, the sample was soaked in 100 mL of concentrated sulfuric acid at 80 °C and 12 M for 4 h. The sample was then repeatedly rinsed with ultrapure water until PH is neutral, then filtered and put into a vacuum drying oven 24 h.

A series of Fe_2O_3/C were synthesized by hydrothermal method with different ratios of Fe_2O_3 and treated rape pollen. Taking Fe_2O_3/C (50% weight of Fe_2O_3) sample as example, 1.28 g of carbonized pollen was added to 171.2 mL mixture solution of ultrapure water and anhydrous ethanol (1.4:20) and ultra-sonicated for 1 h. Then, 4.36 g of $FeCl_3 \cdot 6H_2O$, 12.8 g of anhydrous sodium was added to carbonized pollen suspension. After vigorous stirring for 1 h, the above mixture was transferred to a 100 mL then added to a 100 mL Teflon-lined stainless-steel autoclave and heated at 180 °C for 12 h. The obtained precipitate was separated by centrifugation at 9000 r/min and washed with ethanol and distilled water several times. The resulting solid was dried at 80 °C for 12 h in a vacuum oven.

The samples with a Fe_2O_3 weight ratio of 20%, 50%, and 80% were prepared according to the above procedure and recorded as xFe_2O_3/C. Pure Fe_2O_3 and TRP were also prepared as comparison.

3.2. Characterization of Photocatalysts

The morphology of as-prepared samples was characterized by field emission scanning electron microscope (FESEM, JEOL JSM-7800) and transmission electron microscopy (TEM, JEOL JEM 2100). X-ray diffraction (XRD) patterns were obtained on a PANalyticalX'pert MPD Pro x-ray diffractometer using Ni-filtrated Cu Kα irradiation. UV–vis spectra of the films were collected using a Hitachi U-3900H spectrophotometer in the 300 to 800 nm wavelength range. The sample formation was examined by X-ray photoelectron spectroscope (XPS, AXISULTRA). The BET surface areas and porosity of the samples were deduced from the N_2-adsorption/desorption isotherms at 77 K and the isotherms were determined by using an Accelerated Surface Area and Porosimetry Analyzer (ASAP 2020, Micromeritics, Norcross, GA, USA) after degassing the samples at 105 °C for 6 h.

3.3. Photocatalytic Degradation of MB Conditions

A UV-vis spectrophotometer was used to test the degradation efficiency of MB. Generally, 10 mg/L of the prepared sample was added and dispersed in powder form into 170 mL of MB solution (10 mg/L), the distance between the light source and the reaction system was 25 cm, and before the photocatalytic degradation experiment, the suspension was stirred continuously in the dark for 1 h to reach an adsorption equilibrium between the photocatalyst and the solution. The light source was a 300 W xenon lamp equipped with filter to remove ultraviolet light. During the whole experiment, the suspension was stirred continuously. The temperature of the solution was kept at room temperature by an external cold circulator to prevent the temperature of the experimental environment from increasing due to the light irradiation. The residual concentration of the sample was determined by taking 4 mL of the sample every 30 min, putting it into a centrifuge at high speed, and then taking the supernatant to test the degradation efficiency in a UV-vis spectrophotometer.

3.4. Photocatalytic Disinfection and Microscopic Images of Bacteria

E. coli was incubated in LB broth for 18 h to reach a stable phase of life, and the concentration of the bacteria was adjusted to an OD value of 0.04 at 600 nm using a turbidimetric method to set the initial viable cell density at 10^6 cfu/mL [57]. The bacterial solution was loaded into a double-walled photocatalytic vessel with a circulating cooling water bath, and the photocatalyst was added at a concentration ratio of 100 mg/L. The distance between the light source and the reaction system was 25 cm, the solution was first stirred under dark reaction conditions for 20 min. After the photocatalytic reaction, 1 mL of the bacterial solution was diluted at 0, 20, 40, 60, 80, and 100 min and then coated on LB agar plates. The plates were incubated in a constant temperature incubator at 37 °C for 24 h and then counted. The bactericidal ability of the photocatalyst under photocatalytic conditions was determined by the change in the total number of colonies.

3.5. Microscopic Observation of E. coli

First, 5 mL of the bacterial solution was taken, incubated for 4 h at 37 °C, and centrifuged (8000 r, 10 min, 4 °C), then rinsed twice with phosphate buffer solution (PBS, pH 7.2), followed by fixation with 2 mL of 2.5% glutaraldehyde at 4 °C for 12 h. After fixation, the samples were centrifuged (8000 r, 10 min, 4 °C), rinsed twice with PBS, and dehydrated in an ethanol series (30%, 50%, 70%, 80%, 90%, 100%) gradient dehydration for 10 min in sequence, and finally placed in critical point drying, vacuum gold spray treatment, and observed under SEM.

3.6. Effective ROS Identification

The ROS contributed to MB degradation and the bacterial inactivation process was identified by adding scavengers, including EDTA-2Na for the trap hole (h^+), silver nitrate for trap electron (e^-), isopropanol for trap hydroxyl radical ($\cdot OH$), and 1,4-benzoquinone for trap superoxide radical ($\cdot O_2^-$). The concentration of scavengers was 1 mM. The scavengers were widely used in the photocatalytic system [58] and were proved to have no harmful effect to *E. coli* cells before conducting the scavenger experiments [59]. The experimental processes were according to the photocatalytic bacterial inactivation experiment.

4. Conclusions

A series of Fe_2O_3/TRP photocatalysts were synthesized by a simple hydrothermal method. The composites with 50% mass ratio of Fe_2O_3 exhibited good photodegrade ability and antibacterial ability under light. The improved degradation rate depends on the formation of heterojunctions effectively inhibited the photo-induced recombination of electron-hole pairs, high contact area between sample and solution, and photocatalytic–photothermal effect. This study shows that the hybrid photocatalyst has a great potential to destroy organic pollutants and bacteria under visible light irradiation and provides a new direction for the selection of carbon-based and semiconductor materials.

Author Contributions: Conceptualization, J.J. and H.W.; methodology, Y.M., Y.L. and Y.C.; validation, J.G., Y.M., S.L. and X.L.; formal analysis, J.G. and Y.M.; investigation, J.G. and W.Z.; resources, J.G., X.L. and Y.M.; data curation, J.G., Y.M., S.L. and S.C.; writing—original draft preparation, J.G. and Y.M.; writing—review and editing, R.Z., H.W. and J.J.; project administration, J.J.; funding acquisition, J.J., W.Z. and H.W. All authors have read and agreed to the published version of the manuscript.

Funding: This research was funded by the National Natural Science Foundation of China (No. 12004312, 52002331), and Special research project on the interdisciplinary of fundamental mathematics and physics of Northwest Agriculture and Forestry University (No. 2452022030).

Institutional Review Board Statement: Not applicable.

Informed Consent Statement: Not applicable.

Data Availability Statement: The data used to support the study are included in the article.

Conflicts of Interest: The authors declare no conflict of interest.

References

1. Al Kausor, M.; Chakrabortty, D. Graphene oxide based semiconductor photocatalysts for degradation of organic dye in waste water: A review on fabrication, performance enhancement and challenges. *Inorg. Chem. Commun.* **2021**, *129*, 108630. [CrossRef]
2. Ren, G.; Han, H.; Wang, Y.; Liu, S.; Zhao, J.; Meng, X.; Li, Z. Recent advances of photocatalytic application in water treatment: A review. *Nanomaterials* **2021**, *11*, 1804. [CrossRef] [PubMed]
3. Dong, S.; Cui, L.; Tian, Y.; Xia, L.; Wu, Y.; Yu, J.; Bagley, D.M.; Sun, J.; Fan, M. A novel and high-performance double Z-scheme photocatalyst ZnO-SnO_2-Zn_2SnO_4 for effective removal of the biological toxicity of antibiotics. *J. Hazard. Mater.* **2020**, *399*, 123017. [CrossRef] [PubMed]
4. Zambrano, J.; García-Encina, P.A.; Jiménez, J.J.; López-Serna, R.; Irusta-Mata, R. Photolytic and photocatalytic removal of a mixture of four veterinary antibiotics. *J. Water Process Eng.* **2022**, *48*, 102841. [CrossRef]
5. Lima, M.L.; Romanelli, A.; Massone, H.E. Assessing groundwater pollution hazard changes under different socio-economic and environmental scenarios in an agricultural watershed. *Sci. Total Environ.* **2015**, *530*, 333–346. [CrossRef] [PubMed]
6. Asghar, A.; Lutze, H.V.; Tuerk, J.; Schmidt, T.C. Influence of water matrix on the degradation of organic micropollutants by ozone based processes: A review on oxidant scavenging mechanism. *J. Hazard. Mater.* **2022**, *429*, 128189. [CrossRef] [PubMed]
7. Luo, Z.; He, Y.; Zhi, D.; Luo, L.; Sun, Y.; Khan, E.; Wang, L.; Peng, Y.; Zhou, Y.; Tsang, D.C. Current progress in treatment techniques of triclosan from wastewater: A review. *Sci. Total Environ.* **2019**, *696*, 133990. [CrossRef]
8. Zewde, A.A.; Li, Z.; Zhang, L.; Odey, E.A.; Xiaoqin, Z. Utilisation of appropriately treated wastewater for some further beneficial purposes: A review of the disinfection method of treated wastewater using UV radiation technology. *Rev. Environ. Health* **2022**, *352*, 139–146. [CrossRef] [PubMed]
9. Chen, D.; Cheng, Y.; Zhou, N.; Chen, P.; Wang, Y.; Li, K.; Huo, S.; Cheng, P.; Peng, P.; Zhang, R.; et al. Photocatalytic degradation of organic pollutants using TiO_2-based photocatalysts: A review. *J. Clean. Prod.* **2020**, *268*, 121725. [CrossRef]
10. Song, R.; Chi, H.; Ma, Q.; Li, D.; Wang, X.; Gao, W.; Wang, H.; Wang, X.; Li, Z.; Li, C. Highly efficient degradation of persistent pollutants with 3D nanocone TiO_2-based photoelectrocatalysis. *J. Am. Chem. Soc.* **2021**, *143*, 13664–13674. [CrossRef] [PubMed]
11. Zong, S.; Tian, L.; Guan, X.; Cheng, C.; Shi, J.; Guo, L. Photocatalytic overall water splitting without noble-metal: Decorating CoP on Al-doped $SrTiO_3$. *J. Colloid Interf. Sci.* **2022**, *606*, 491–499. [CrossRef]
12. Ali, A.M.; Sayed, M.A.; Algarni, H.; Ganesh, V.; Aslam, M.; Ismail, A.A.; El-Bery, H.M. Synthesis, characterization and photoelectric properties of Fe_2O_3 incorporated TiO_2 photocatalyst nanocomposites. *Catalysts* **2021**, *11*, 1062. [CrossRef]
13. Asif, A.H.; Wang, S.; Sun, H. Hematite-based nanomaterials for photocatalytic degradation of pharmaceuticals and personal care products (PPCPs): A short review. *Curr. Opin. Green Sustain. Chem.* **2021**, *281*, 100447. [CrossRef]
14. Katoch, V.; Sharma, N.; Sharma, M.; Baghoria, M.; Panda, J.J.; Singh, M.; Prakash, B. Microflow synthesis and enhanced photocatalytic dye degradation performance of antibacterial Bi_2O_3 nanoparticles. *Environ. Sci. Pollut. Res.* **2021**, *2815*, 19155–19165. [CrossRef] [PubMed]
15. Bhavsar, K.S.; Labhane, P.K.; Dhake, R.B.; Sonawane, G.H. Solvothermal synthesis of activated carbon loaded CdS nanoflowers: Boosted photodegradation of dye by adsorption and photocatalysis synergy. *Chem. Phys. Lett.* **2020**, *744*, 137202. [CrossRef]
16. Sharma, B.; Boruah, P.K.; Yadav, A.; Das, M.R. TiO_2–Fe_2O_3 nanocomposite heterojunction for superior charge separation and the photocatalytic inactivation of pathogenic bacteria in water under direct sunlight irradiation. *J. Environ. Chem. Eng.* **2018**, *6*, 134–145. [CrossRef]
17. Sze-Mun, L.; Man-Kit, C.; Jin-Chung, S.; Honghu, Z.; Liangliang, H.; Lin, H.; Haixiang, L.; Haider, J.Z.; Hwa, C.K. Construction of delaminated Ti_3C_2 MXene/$NiFe_2O_4$/V_2O_5 ternary composites for expeditious pollutant degradation and bactericidal property. *J. Environ. Chem. Eng.* **2022**, *10*, 108284.
18. Liu, H.; Zhang, Z.; Wang, X.; Nie, G.; Zhang, J.; Zhang, S.; Cao, N.; Yan, S.; Long, Y. Highly flexible Fe_2O_3/TiO_2 composite nanofibers for photocatalysis and ultraviolet detection. *J. Phys. Chem. Solids* **2018**, *121*, 236–246. [CrossRef]

19. Hu, X.; Han, S.; Zhu, Y. Facet-controlled synthesis of polyhedral hematite/carbon composites with enhanced photoactivity. *Appl. Surf. Sci.* **2018**, *443*, 227–235. [CrossRef]
20. Khasawneh, O.; Palaniandy, P. Removal of organic pollutants from water by Fe_2O_3/TiO_2 based photocatalytic degradation: A review. *Environ. Technol. Innov.* **2021**, *21*, 101–230.
21. Zhu, D.; Zhang, J.; Song, J.; Wang, H.; Yu, Z.; Shen, Y.; Xie, A. Efficient one-pot synthesis of hierarchical flower-like α-Fe_2O_3 hollow spheres with excellent adsorption performance for water treatment. *Appl. Surf. Sci.* **2013**, *284*, 855–861. [CrossRef]
22. Ji, M.; Cai, J.; Ma, Y.; Qi, L. Controlled growth of ferrihydrite branched nanosheet arrays and their transformation to hematite nanosheet arrays for photoelectrochemical water splitting. *ACS Appl. Mater. Inter.* **2016**, *86*, 3651–3660. [CrossRef] [PubMed]
23. Samanta, A.; Das, S.; Jana, S. Doping of Ni in α-Fe_2O_3 nanoclews to boost oxygen evolution electrocatalysis. *ACS Sustain. Chem. Eng.* **2019**, *7*, 12117–12124. [CrossRef]
24. Zhang, W.; Chen, H.; Zhang, L.; Zhang, P.; Dong, E.; Ma, J.; Wang, G. Design and fabrication of an α-Fe_2O_3/TiO_2/Si 3D hierarchical photoanode for improved photoelectrochemical water splitting. *J. Alloys Compd.* **2019**, *773*, 597–604. [CrossRef]
25. Gong, H.; Zhao, C.; Niu, G.; Zhang, W.; Wang, F. Construction of 1D/2D α-Fe_2O_3/SnO_2 hybrid nanoarrays for sub-ppm acetone detection. *Research* **2020**, *2020*, 2196063. [CrossRef] [PubMed]
26. Ahmed, A.M.; Shaban, M. Highly sensitive Au-Fe_2O_3-Au and Fe_2O_3-Au-Fe_2O_3 biosensors utilizing strong surface plasmon resonance. *Appl. Phys. B* **2020**, *126*, 57. [CrossRef]
27. Lakhera, S.K.; Venkataramana, R.; Watts, A.; Anpo, M.; Neppolian, B. Facile synthesis of Fe_2O_3/Cu_2O nanocomposite and its visible light photocatalytic activity for the degradation of cationic dyes. *Res. Chem. Intermed.* **2017**, *43*, 5091–5102. [CrossRef]
28. Narendhran, S.; Shakila, P.B.; Manikandan, M.; Vinoth, V.; Rajiv, P. Spectroscopic investigation on photocatalytic degradation of methyl orange using $Fe_2O_3/WO_3/FeWO_4$ nanomaterials. *Spectrochim. Acta A* **2020**, *232*, 118164. [CrossRef] [PubMed]
29. Feng, C.; Fu, H.; Jia, H.; Jin, H.; Cheng, X.; Wang, W.; Liu, M.; Zhou, Q. Ultrathin Ti_3C_2 nanosheets served as a highly efficient hole transport layer on a Fe_2O_3 photoanode for photoelectrochemical water oxidation. *New J. Chem.* **2021**, *45*, 20537–20541. [CrossRef]
30. Fard, A.K.; Mckay, G.; Preud'Homme, H.; Kochkodan, V.; Atieh, M.A. Fabrication and evaluation of activated carbon/Fe_2O_3 nano-composite on the removal of strontium ions from water. *Desalin. Water Treat.* **2017**, *73*, 399–408. [CrossRef]
31. Muhajir, M.; Puspitasari, P.; Razak, J.A. Synthesis and applications of Hematite α-Fe_2O_3: A Review. *J. Mech. Eng. Sci.* **2020**, *3*, 51–58. [CrossRef]
32. Zhang, P.; Sun, B.; Wu, F.; Zhang, Q.; Chu, X.; Ge, M.; Zhou, N.; Shen, J. Wound healing acceleration by antibacterial biodegradable black phosphorus nanosheets loaded with cationic carbon dots. *J. Mater. Sci.* **2021**, *56*, 6411–6426. [CrossRef]
33. Sahani, S.; Tripathi, K.M.; Lee, T.I.; Dubal, D.P.; Wong, C.P.; Sharma, Y.C.; Kim, T.Y. Recent advances in photocatalytic carbon-based materials for enhanced water splitting under visible-light irradiation. *Energ. Convers. Manag.* **2022**, *252*, 115133. [CrossRef]
34. Xu, J.; Yao, Q.; Li, P.; Zhang, X.; Wang, S.; Pan, C. Construction of amorphous carbon-coated alpha-Fe_2O_3 core–shell nanostructure for efficient photocatalytic performance. *J. Mater. Sci. Mater. Electron.* **2022**, *33*, 22549–22559. [CrossRef]
35. Sun, P.; Zhou, S.; Yang, Y.; Liu, S.; Cao, Q.; Wang, Y.; Wagberg, T.; Hu, G. Artificial chloroplast-like phosphotungstic acid-iron oxide microbox heterojunctions penetrated by carbon nanotubes for solar photocatalytic degradation of tetracycline antibiotics in wastewater. *Adv. Compos. Hybrid Mater.* **2022**, *5*, 3158–3175. [CrossRef]
36. Sun, S.; Sun, M.; Kong, Y.; Fang, Y.; Yao, Y. MoS_2 and graphene as dual, cocatalysts for enhanced visible light photocatalytic activity of Fe_2O_3. *J. Sol-Gel Sci. Technol.* **2016**, *80*, 719–727. [CrossRef]
37. Shin, J.; Hutomo, C.A.; Kim, J.; Jang, J.; Park, C.B. Natural pollen exine-templated synthesis of photocatalytic metal oxides with high surface area and oxygen vacancies. *Appl. Surf. Sci.* **2022**, *599*, 154064. [CrossRef]
38. Xia, D.; Chen, Q.; Jiao, Y.; Lian, Q.; Sun, M.; He, C.; Shang, J.; Wang, T. A modified flower pollen-based photothermocatalytic process for enhanced solar water disinfection: Photoelectric effect and bactericidal mechanisms. *Water Res.* **2022**, *217*, 118423. [CrossRef] [PubMed]
39. He, B.; Feng, M.; Chen, X.; Zhao, D.; Sun, J. One-pot construction of chitin-derived carbon/g-C_3N_4 heterojunction for the improvement of visible-light photocatalysis. *Appl. Surf. Sci.* **2020**, *527*, 146737. [CrossRef]
40. Sun, J.; Zhang, J.; Zhang, M.; Antonietti, M.; Fu, X.; Wang, X. Bioinspired hollow semiconductor nanospheres as photosynthetic nanoparticles. *Nat. Commun.* **2012**, *3*, 1139. [CrossRef]
41. Jiang, Z.; Sun, H.; Wang, T.; Wang, B.; Wei, W.; Li, H.; Yuan, S.; An, T.; Zhao, H.; Yu, J.; et al. Nature-based catalyst for visible-light-driven photocatalytic CO_2 reduction. *Energy Environ. Sci.* **2018**, *11*, 2382–2389. [CrossRef]
42. Xu, Q.; Zhu, B.; Jiang, C.; Bei, C.; Yu, J. Constructing 2D/2D Fe_2O_3/g-C_3N_4 direct Z-scheme photocatalysts with enhanced H_2 generation performance. *Sol. RRL* **2018**, *2*, 1800006. [CrossRef]
43. Priyadharsan, A.; Vasanthakumar, V.; Shanavas, S.; Karthikeyan, S.; Anbarasan, P. Crumpled sheet like graphene based WO_3-Fe_2O_3 nanocomposites for enhanced charge transfer and solar photocatalysts for environmental remediation. *Appl. Surf. Sci.* **2019**, *470*, 114–128. [CrossRef]
44. Pradhan, G.; Padhi, D.; Parida, K. Fabrication of α-Fe_2O_3 Nanorod/RGOcomposite: A novel hybrid photocatalyst for phenol degradation. *ACS Appl. Mater. Interf.* **2013**, *5*, 9101–9110. [CrossRef] [PubMed]
45. She, X.; Wu, J.; Xu, H.; Zhong, J.; Ajayan, P.M. High efficiency photocatalytic water splitting using 2D α-Fe_2O_3/g-C_3N_4 Z-scheme catalysts. *Adv. Energy Mater.* **2017**, *7*, 170025. [CrossRef]
46. Feng, H.; Wang, W.; Zhang, M.; Zhu, S.; Wang, Q.; Liu, J.; Chen, S. 2D titanium carbide-based nanocomposites for photocatalytic bacteriostatic applications. *Appl. Catal. B Environ.* **2020**, *266*, 118609. [CrossRef]

47. Wei, Y.; Wang, Z.; Su, J.; Guo, L. Metal-Free Flexible Protonated g-C_3N_4/Carbon Dots Photoanode for Photoelectrochemical Water Splitting. *ChemElectroChem* **2018**, *5*, 2734–2737. [CrossRef]
48. Li, X.; Chen, D.; Li, N.; Xu, Q.; Li, H.; He, J.; Lu, J. Efficient reduction of Cr (VI) by a BMO/Bi_2S_3 heterojunction via synergistic adsorption and photocatalysis under visible light. *J. Hazard. Mater.* **2020**, *400*, 123243. [CrossRef]
49. Nikitenko, S.I.; Chave, T.; Cau, C.; Brau, H.P.; Flaud, V. Photothermal hydrogen production using noble-metal-free Ti@TiO_2 core–shell nanoparticles under visible–NIR light irradiation. *ACS Catal.* **2015**, *5*, 4790–4795. [CrossRef]
50. Jiang, R.; Wu, D.; Lu, G.; Yan, Z.; Liu, J. Modified 2D-2D $ZnIn_2S_4$/BiOCl van der Waals heterojunctions with CQDs: Accelerated charge transfer and enhanced photocatalytic activity under vis-and NIR-light. *Chemosphere* **2019**, *227*, 82–92. [CrossRef]
51. Wang, C.; Li, J.; Liu, X.; Cui, Z.; Chen, D.F.; Li, Z.; Liang, Y.; Zhu, S.; Wu, S. The rapid photoresponsive bacteria-killing of Cu-doped MoS_2. *Biomater. Sci.* **2020**, *8*, 4216–4224. [CrossRef]
52. Rajendran, A.; Alsawalha, M.; Alomayri, T. Biogenic synthesis of husked rice-shaped iron oxide nanoparticles using coconut pulp (*Cocos nucifera* L.) extract for photocatalytic degradation of rhodamine b dye and their in vitro antibacterial and anticancer activity. *J. Saudi Chem. Soc.* **2021**, *25*, 101307. [CrossRef]
53. Haseena, S.; Shanavas, S.; Duraimurugan, J.; Ahamad, T.; Jayamani, N. Study on photocatalytic and antibacterial properties of phase pure fe2o3 nanostructures synthesized using caralluma fimbriata and achyranthes aspera leaves. *Optik* **2020**, *203*, 164047. [CrossRef]
54. Tharani, K.; Christy, A.J.; Sagadevan, S.; Nehru, L.C. Photocatalytic and antibacterial performance of iron oxide nanoparticles formed by the combustion method. *Chem. Phys. Lett.* **2021**, *771*, 138524. [CrossRef]
55. Xiao, K.; Wang, T.; Sun, M.; Hanif, A.; Gu, Q.; Tian, B.; Jiang, Z.; Wang, B.; Sun, H.; Shang, J.; et al. Photocatalytic bacterial inactivation by a rape pollen-MoS_2 biohybrid catalyst: Synergetic effects and inactivation mechanisms. *Environ. Sci. Technol.* **2019**, *54*, 537–549. [CrossRef] [PubMed]
56. Wang, B.; Jiang, Z.; Jimmy, C.Y. Treated rape pollen: A metal-free visible-light-driven photocatalyst from nature for efficient water disinfection. *J. Mater. Chem. A* **2019**, *7*, 9335–9344. [CrossRef]
57. Liu, F.; Nie, C.; Dong, Q.; Ma, Z.; Liu, W.; Tong, M. AgI modified covalent organic frameworks for effective bacterial disinfection and organic pollutant degradation under visible light irradiation. *J. Hazard. Mater.* **2020**, *398*, 122865. [CrossRef]
58. Liu, Y.; Zeng, X.; Easton, C.D.; Li, Q.; Xia, Y.; Yin, Y.; Hu, X.; Hu, J.; Xia, D.; McCarthy, D.T.; et al. An in situ assembled WO_3–TiO_2 vertical heterojunction for enhanced Z-scheme photocatalytic activity. *Nanoscale* **2020**, *12*, 8775–8784. [CrossRef] [PubMed]
59. Liang, J.; Liu, F.; Li, M.; Liu, W.; Tong, M. Facile synthesis of magnetic Fe_3O_4@BiOI@AgI for water decontamination with visible light irradiation: Different mechanisms for different organic pollutants degradation and bacterial disinfection. *Water Res.* **2018**, *137*, 120–129. [CrossRef]

Disclaimer/Publisher's Note: The statements, opinions and data contained in all publications are solely those of the individual author(s) and contributor(s) and not of MDPI and/or the editor(s). MDPI and/or the editor(s) disclaim responsibility for any injury to people or property resulting from any ideas, methods, instructions or products referred to in the content.